Article

Controlled Transition Metal Nucleated Growth of Carbon Nanotubes by Molten Electrolysis of CO$_2$

Xinye Liu [1], **Gad Licht** [2], **Xirui Wang** [1] and **Stuart Licht** [1,2,*]

[1] Department of Chemistry, George Washington University, Washington, DC 20052, USA; xyl@gwmail.gwu.edu (X.L.); xiruiwang@email.gwu.edu (X.W.)
[2] C2CNT, Carbon Corp, 1035 26 St NE, Calgary, AB T2A 6K8, Canada; glicht@wesleyan.edu
[*] Correspondence: slicht@gwu.edu

Abstract: The electrolysis of CO$_2$ in molten carbonate has been introduced as an alternative mechanism to synthesize carbon nanomaterials inexpensively at high yield. Until recently, CO$_2$ was thought to be unreactive, making its removal a challenge. CO$_2$ is the main cause of anthropogenic global warming and its utilization and transformation into a stable, valuable material provides an incentivized pathway to mitigate climate change. This study focuses on controlled electrochemical conditions in molten lithium carbonate to split CO$_2$ absorbed from the atmosphere into carbon nanotubes (CNTs), and into various macroscopic assemblies of CNTs, which may be useful for nanofiltration. Different CNT morphologies were prepared electrochemically by variation of the anode and cathode composition and architecture, variation of the electrolyte composition pre-electrolysis processing, and variation of the current application and current density. Individual CNT morphologies' structures and the CNT molten carbonate growth mechanisms are explored using SEM (scanning electron microscopy), TEM (transmission electron micrsocopy), HAADF (high angle annular dark field), EDX (energy dispersive xray), X-ray diffraction), and Raman methods. The principle commercial technology for CNT production had been chemical vapor deposition, which is an order of magnitude more expensive, generally requires metallo-organics, rather than CO$_2$ as reactants, and can be highly energy and CO$_2$ emission intensive (carries a high carbon positive, rather than negative, footprint).

Keywords: nanocarbon; carbon nanotubes; carbon dioxide electrolysis; molten carbonate; greenhouse gas mitigation

1. Introduction

Global CO$_2$ has risen rapidly, accelerating extinction risk [1–4]. CO$_2$ is a highly stable molecule and is difficult to remove from the environment [5]. One means to mitigate CO$_2$ under consideration is its low-energy chemical transformation to a (i) stable, (ii) useful, and (iii) valuable product, with a low cost and low carbon footprint of production. The transformed CO$_2$'s product stability prevents the captured CO$_2$ from re-emission, the product's usefulness provides a buffer to store the captured carbon, and its high-value (ideally higher than the cost of CO$_2$ transformation) provides an economic incentive to remove the greenhouse gas. Graphitic nanocarbons, such as carbon nanotubes made from CO$_2$, may meet several of these transformed CO$_2$ product requirements. For example, its basic structure of layered graphene retains the durability of graphite, whose hundreds-of-millions-year-old mineral deposits attest to its long term stability, while CNTs' market value of $100,000 to $400,000/tonne can provide a revenue, rather than a cost, while removing CO$_2$.

Multiwalled CNTs (Carbon NanoTubes) are comprised of concentric cylindrical graphene sheets. CNTs have a measured tensile strength of 93,900 MPa, which is the highest tensile strength of any material [6,7]. Other useful properties of CNTs include high electrical capacity, high thermal conductivity, high flexibility, high capacity for charge storage, and catalysis. CNTs applications range from stronger, lighter structural materials including cement,

aluminum, and steel admixtures [8], to medical applications [9,10], electronics, batteries and supercapacitors [11,12], sensors and analysis [13–15], plastics and polymers [16–20], textiles [21], hydrogen storage [22], and water treatment [23,24].

The deliberate thought of this study is that the superior physical chemical properties of CNTs, and in particular CNTs made by consuming CO_2, will cause a demand for its application, thereby incentivizing CO_2 consumption and driving climate change mitigation by decreasing emissions of the greenhouse gas CO_2.
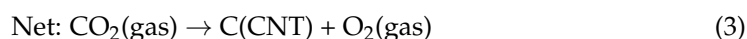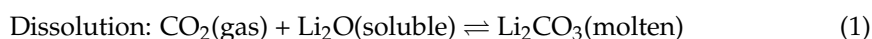
Increased pathways for the use of CO_2 as a molten carbonate electrolysis reactant to synthesize value-added CNTs will provide the effect of opening a path to consume this greenhouse gas to mitigate climate change, and its transformation to CNTs will provide a stable material to store carbon removed from the environment.

To date, the CNT market has been limited due to a high cost of production. Commercially, CNTs are mainly produced by chemical vapor deposition (CVD) and not from CO_2 [25,26]. CVD production of CNTs is chemical and energy intensive and expensive, leading to current costs of \$100 K to \$400 K per tonne of CNT, and CVD production has a high carbon footprint [27].

Prior attempts to transform CO_2 to carbon nanotubes or graphene have been low yield and energy intensive, such as the production of graphitic flakes using high-pressure CO_2 or by electrolysis in molten $CaCl_2$ electrolytes. Undesired byproducts included Al_2O_3, hydrogen, and hydrocarbons, and from the electrolysis, carbon monoxide byproducts from an 850 °C electrolysis splitting in molten $CaCl_2$ electrolytes [28,29].

However, CO_2 has a strong affinity for certain molten carbonates. In 2009, a process was introduced to mitigate the greenhouse gas CO_2 through molten electrolytic splitting and transformation at elevated temperatures. Pathways were opened to the high-purity, renewable energy electrolytic splitting of CO_2 to solid carbon by demonstrating that in molten lithium carbonate (melting point 723 °C) electrolytes, the four-electron molten electrolysis reduction of tetravalent carbon to solid products dominates below 800 °C. With rising electrolysis temperature between 800 and 900 °C, the two-electron reduction to a CO product increasingly dominates, and by 950 °C, the transition to the alternative CO byproduct is complete [30].

The solid carbon product of CO_2 electrolysis was further refined to graphitic nanocarbons through the discovery of the catalyzed molten electrolysis transition metal nucleated growth of carbon nanotubes and carbon nanofibers in lithium carbonate electrolytes [31–33]. The process was given the acronym C2CNT (Carbon dioxide to Carbon NanoTubes). The ^{13}C isotope of CO_2 was used to track carbon through the C2CNT process from its origin (CO_2 as a gas phase reactant) through its transformation to a CNT or carbon nanofiber product, and the CO_2 originating from the gas phase served as the renewable C building blocks in the observed CNT product [32]. The net reaction is:

$$\text{Dissolution: } CO_2(\text{gas}) + Li_2O(\text{soluble}) \rightleftharpoons Li_2CO_3(\text{molten}) \tag{1}$$

$$\text{Electrolysis: } Li_2CO_3(\text{molten}) \rightarrow C(\text{CNT}) + Li_2O \text{ (soluble)} + O_2(\text{gas}) \tag{2}$$

$$\text{Net: } CO_2(\text{gas}) \rightarrow C(\text{CNT}) + O_2(\text{gas}) \tag{3}$$

The electrolytic CO_2 splitting in molten carbonates could occur at electrolysis potentials of less than 1 volt [33]. Due to the high affinity of CO_2 towards reaction 1, that is, for the Li_2O present in the electrolyte, in the C2CNT process, the electrolytic splitting could occur as a direct capture of carbon in the air without CO_2 pre-concentration, or with exhaust gas, or with concentrated CO_2. As it directly captured CO_2 from the air, no further introduction of CO_2 was needed throughout the group's experiments. By means of variation of the electrolysis setup, the process could produce, in addition to conventional morphology CNT: doped CNTs, helical CNTs, and magnetic CNTs, as illustrated in Figure 1 [31–44]. Studied applications of electrolytic CNTs from CO_2 include batteries [34], CO_2 transformation from power station flue gas [45], and the substantial decrease in the carbon footprint of structural materials as CNT composites, including CNT-cement, CNT-steel, and CNT-

aluminum [8,46], as well as modification of the CO_2 splitting process to yield other CNMs including carbon nano-onions, carbon platelets, and graphene [47–51].
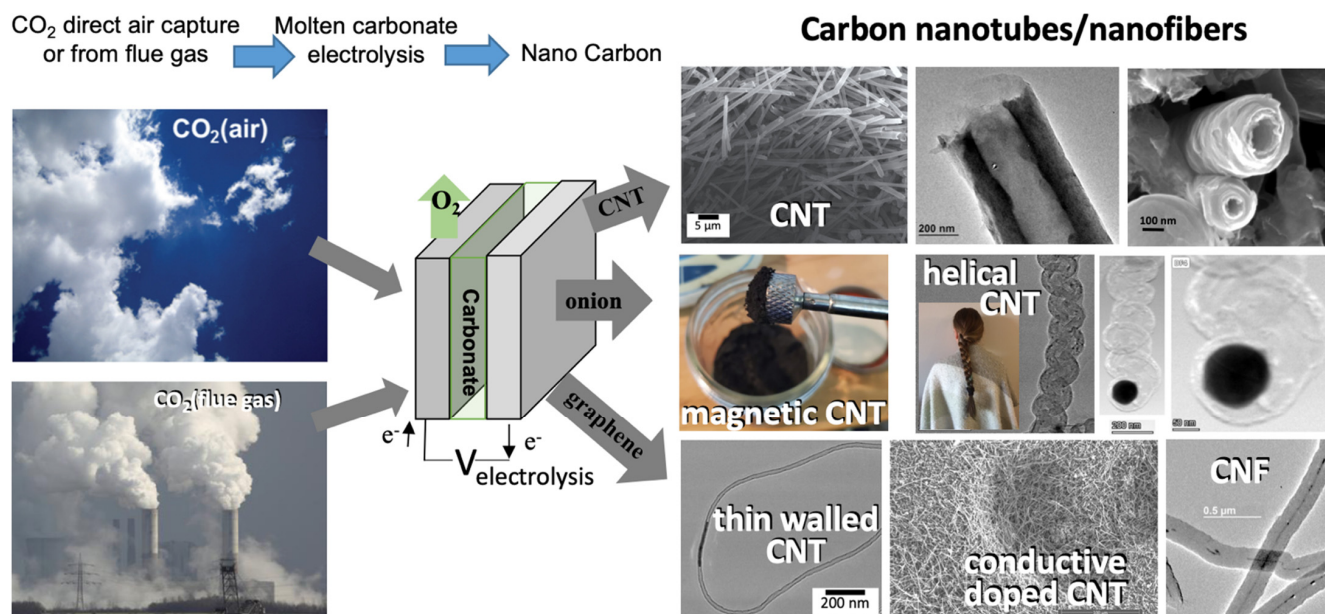

Figure 1. High-yield electrolytic synthesis of carbon nanotubes from CO_2, either directly from the air or from smokestack CO_2, in molten carbonate.

The rise of this greenhouse gas is causing extensive climate change and damage to the planet's ecosphere, and its mitigation is one of the most pressing challenges of our time [1–5]. Technical, catalyst-driven solutions to mitigate climate change are of the highest significance to the catalyst, not only due to their probes of a new chemistry to catalyze nanocarbon formation, but also by galvanizing the community with action towards mitigation of the existential climate change threat facing the planet. This study provides four contributions to a catalyst-driven solution to climate change: (i) Ten distinct, new electrochemical procedures are presented to transform CO_2 to CNTs at high purity. The procedures produce a variety of distinct CNT morphologies ranging from curled to straight, short to long, and thin to thick. (ii) This study explores the transition metal nucleation that catalyzes the process to produce high-purity carbon nanotubes. (iii) The study demonstrates new syntheses of macroscopic assemblies of CNTs using the C2CNT process, with structural implications towards their potential applications for nano-filtration and neural nets. (iv) This study provides an extensive carbon nanotube baseline to a companion study in which the same electrochemical components are utilized in new configurations to generate entire new classes of non-carbon nanotube graphitic nanocarbons.

2. Results and Discussion

2.1. Electrolytic Conditions to Synthesize High-Purity, High-Yield CNTs from CO_2

The first part of this study systematically explores electrochemical parameters to reveal a wide variety of conditions that yield a high-purity, high-yield CNT product by means of electrolysis of CO_2 in 770 °C lithium carbonate. An in depth look at the material composition and morphologies of the products is conducted, particularly around the transition metal nucleation zone of CNT growth. The latter part of this study reveals molten electrochemical conditions that produce macroscopic assemblies of CNTs. This study also serves as a sister study [51] in which small electrolytic changes in the 770 °C molten Li_2CO_3 yield major changes to the product consisting of new, non-CNT nanocarbon allotropes.

Previously, we showed that the high production rate (using a high electrolysis current density, J, of 0.6 A/cm^2) electrolytic splitting of CO_2 in molten Li_2CO_3 electrolyte using a Muntz Brass cathode (60% Cu and 40% Zn) and a Nichrome C (60% Ni, 24% Fe and

16% Cr) anode produced a high-quality (97% purity), high-aspect-ratio carbon nanotube (CNT) product with the addition, to the electrolyte, of either 0.1 wt% Fe_2O_3 [43] or 2.0 wt% Li_2O [41,44]. The addition of higher concentrations of either iron or lithium oxide to the electrolyte increased the formation of defects in the CNTs, as measured by Raman spectroscopy, which at this higher current density induced spiraling of the CNT during growth and the controlled growth of a variety of helical carbon nano-allotropes including single- and double-braided helices was observed, as well as flat, spiral morphologies [43,44].

Here, conditions related to the high-purity CNT synthesis were systematically varied to determine other electrochemical conditions that support the high-purity, low-defect formation of straight (non-helical) CNTs. Examples of the conditions that were varied include the composition of the cathode and anode, the additives to the lithium carbonate electrolyte, and the current density and time of the electrolysis. Variations of the electrodes include the use of cathode metal electrodes such as Muntz brass Monel, or Nichrome alloys. Anode variations include noble anodes such as iridium, various nickel-containing anodes including nickel, Nichrome A or C, Inconel 600, 625, or 718, or specific layered combinations of these metals. Electrolyte additives that were varied include Fe_2O_3, and nickel or chromium powder, and electrolyses were varied over a wide range of electrolysis current densities. Several electrolyses studied here, which yielded high-purity, high-yield carbon nanotubes, are described in Table 1. Scanning electron microscopy (SEM) of the products of a variety of those CNT syntheses was conducted by CO_2 electrolysis in molten Li_2CO_3 at 770 °C, and the results are presented in Figure 2.

Table 1. A variety of Electrolytic CO_2 splitting conditions in 770 °C Li_2CO_3 producing a high yield of carbon nanotubes.

| Electrolysis	Cathode	Anode	Additives (wt% Powder)	Electr Time	Current Density A/cm^2	Product Description
A	Muntz Brass	Nichrome C	0.1% Fe_2O_3	0.5 h	0.6	97% Straight 50–100 µm CNT
B	Muntz Brass	Nichrome A	0.1% Fe_2O_3	4 h	0.15	94% Straight 20–80 µm CNT
C	Muntz Brass	Inconel 718	0.1% Fe_2O_3 0.1% Ni	4 h	0.15	96% curled CNT
D	Muntz Brass	Nichrome C	0.1% Fe_2O_3	15 h	0.08	70% 10–30 µm CNT
E	Muntz Brass	Inconel 625 3 layers Inconel 600	0.1% Fe_2O_3	15 h	0.08	97% 20–50 µm CNT
F	Muntz Brass	Inconel 718 2 layers Inconel 600	0.1% Fe_2O_3	4 h	0.15	98% Straight 100–500 µm CNT
G	Muntz Brass	Inconel 718 3 layers Inconel 600	0.1% Fe_2O_3 0.1% Ni	15 h	0.08	90% Curled CNT or fibers
H	Muntz Brass	Nichrome C	0.1% Fe_2O_3	1 h	0.4	96% Straight 100–200 µm CNT
I	Monel	Nichrome C	0.1% Fe_2O_3	1 h	0.4	97% Straight 20–50 µm CNT
J	Monel	Nickel	/	2 h	0.2	70% thin 10–20 µm CNT Rest: Onions
K	Monel	Nichrome C	0.1% Fe_2O_3	2 h	0.1	97% 30–60 µm straight CNT
L	Monel	Nichrome C	0.5% Fe_2O_3	15 h	0.08	~25% curled CNT ~70% straight CNT
M	Monel	Iridium	0.81% Cr	18 h	0.08	97% thin 50–100 µm CNT
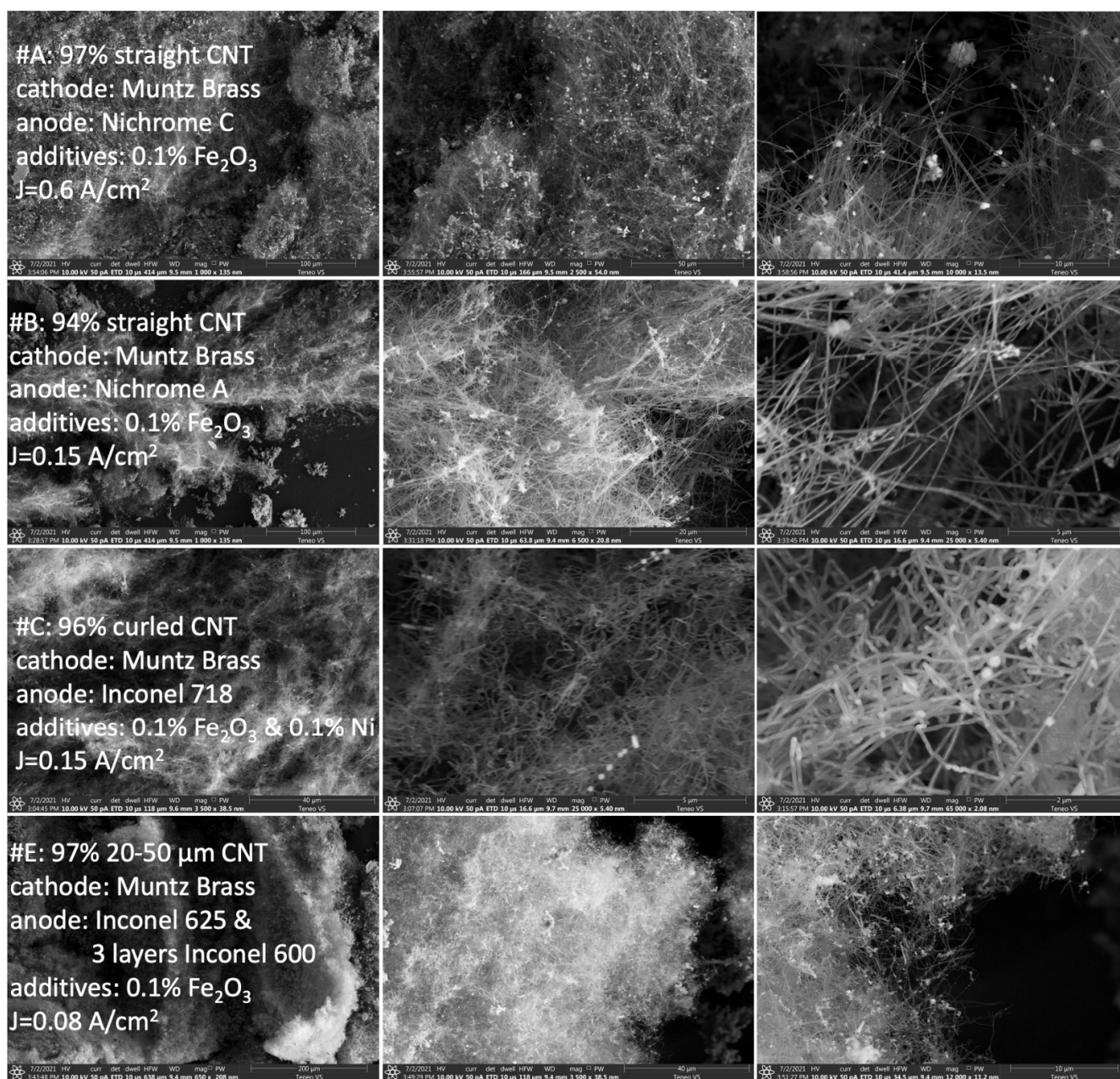
Figure 2. SEM of the synthesis product of high-purity, high-yield carbon nanotubes under a variety of electrochemical conditions by electrolytic splitting of CO_2 in 770 °C Li_2CO_3. The washed product was collected from the cathode subsequent to the electrolysis described in Table 1. Moving left to right in the panels, the product was analyzed by SEM with increasing magnification. Scale bars in panels (starting from left) are for panels A: 100, 50, and 10 μm; for panels B: 100, 20, and 5 μm; for panels C: 40, 5, and 2 μm; for panels E: 200, 40, and 10 μm.

For Electrolysis A, the top row of Table 1 presents the electrochemical conditions, and the top row of Figure 2 presents the SEM results of the product of a repeat of the electrochemical conditions of the described 0.1 wt% Fe_2O_3 electrolysis (the same lithium carbonate electrolyte, the same Muntz Brass cathode and Nichrome C anode, and the same 0.6 A/cm^2 current density and 30 min electrolysis duration), but used a simpler (from a material perspective) alumina (ceramic Al_2O_3), rather than stainless steel 304 electrolysis cell casing. Use of the alumina casing in this study limited the pathways for metals to enter, thereby the reducing parameters to evaluate, and possibly effect, the electrolytic system. Note, however, that the stainless steel 304 was not observed to corrode, and the switch

from stainless to alumina was not observed to materially affect the electrolysis product. The CNT product was again 97% purity, and the coulombic efficiency was 99%, which quantified the measured available charge (current multiplied by the electrolysis time) to the measured number of four electrons per equivalent of C in the product, and the carbon nanotube length was 50 to 100 μm.

The second row of Figure 2 (panels B) represents a change only in the current density, which was lowered to 0.15 A/cm^2, and the electrolysis time, which was increased to 4 h, and the result was a decrease in product purity to 94%, a decrease in CNT length to 20–80 μm, and a modest decrease in coulombic efficiency to 98%. At this current density, as observed in the third row of Figure 2, panels C, the addition of 0.1 wt% Ni along with the 0.1 wt% Fe$_2$O$_3$ resulted in 96% purity, zigzag-patterned and twisted, rather than straight CNTs. These twists could be induced by over-nucleation decreasing control of the CNT linear growth. In the most magnified of these product images (right side of the Figure, 2 μm bar resolution), evidence of the over-nucleation can be observed in the larger nodules visible at the CNT tips and joints.

At a low current density of 0.08 A/cm^2, with an electrolyte additive of 0.1 wt% Fe$_2$O$_3$, the conventional Muntz Brass and Nichrome electrodes exhibited a significant drop in CNT product purity to 70%. Coulombic efficiency tended to drop off with current density, and, in this case, the coulombic efficiency of the synthesis was 82%. Product purity could be increased by refining the mix of transition metals available to the electrolytes or increasing the surface area. The alloy compositions of the metals used as electrodes are presented in Table 2. The metal variation was further refined by combining the metals in Table 2 as anodes; for example, using a solid sheet of one Inconel alloy, layered with a screen or screens of another Inconel alloy. This approach was utilized to obtain the results shown in the lowest row of Figure 2 (panels E); an anode of Inconel 625 with three layers of (spot welded) 100-mesh Inconel 600 screen, a return to a single electrolyte additive (0.1 wt% Fe$_2$O$_3$), and a very low current density of 0.08 A/cm^2 were utilized. As seen in panels E of the figure, the product was high purity (97%) and consisted of 20–50 μm length CNTs, and the coulombic efficiency was 75%. Not shown, but included in Table 1 (Electrolysis G), are the results obtained under the same electrode, and the same 0.08 A/cm^2 electrolysis conditions. However, with the electrolyte addition of both 0.1 wt% Fe$_2$O$_3$ and 0.1 wt% Ni at J = 0.15 A/cm^2, the product was twisted CNTs as shown in Figure 2 panels C, the purity was 96%, and the coulombic efficiency was 80%.

Table 2. Compositions of various alloys used (weight percentage).

Alloy	Ni %	Fe %	Cu %	Zn %	Cr %	Mo %	Nb & Ta %
Nichrome C	60	24			16		
Nichrome A	80				20		
Inconel 600	52.5	18.5			19.0	3.0	3.6
Inconel 718	72% min	6–10			14–17		
Inconel 625	58	5 max			20–23	8–10	4.15–3.15
Monel	67		31.5				
Muntz Brass			60	40			

2.2. Electrolytic Conditions to Synthesize High-Purity, High-Yield CNTs from CO$_2$

The syntheses listed in Table 1 delineated the electrochemical growth conditions for the high-purity growth of carbon nanotubes, each exhibiting the characteristic concentric multiple-graphene cylindrical walls. This can be observed in Figure 3, which presents Transmission Electron Microscopy (TEM) and High Angle Annular Dark-Field TEM (HAADF) results of a typical example (the product of Electrolysis E, as further described in Table 1 and Figure 2), and which provides general structural and mechanistic information of carbon nanotubes synthesized by molten electrolysis. As seen in the top row of the figure, the carbon nanotubes were formed by successive, concentric layers of cylindrical graphene. The graphene can be identified by its characteristic inter-graphene layer separation of

0.33 to 0.34 nm as measured in the figure by the spacing between the dark layers of uniform blocked electron transmission on the magnified top right side of the figure. This CNT had an outer diameter of 74 nm, and inner diameter of 46 nm, and by counting dark rows, it can be determined that the number of graphene layers in this CNT was 41. The right side of the third row of the figure measures the carbon elemental profile of the CNT. This profile was swept laterally from the tube's exterior (no carbon) through the left wall (carbon), then through the void of interior of the tube (low carbon from the exterior backside wall), then through the right wall (carbon), and finally to the exterior of the tube on the outer left side (no carbon). Additionally, the integrated elemental profile of area 1 of this panel is shown, which exhibits 100.0% carbon (fit error 1.3%).
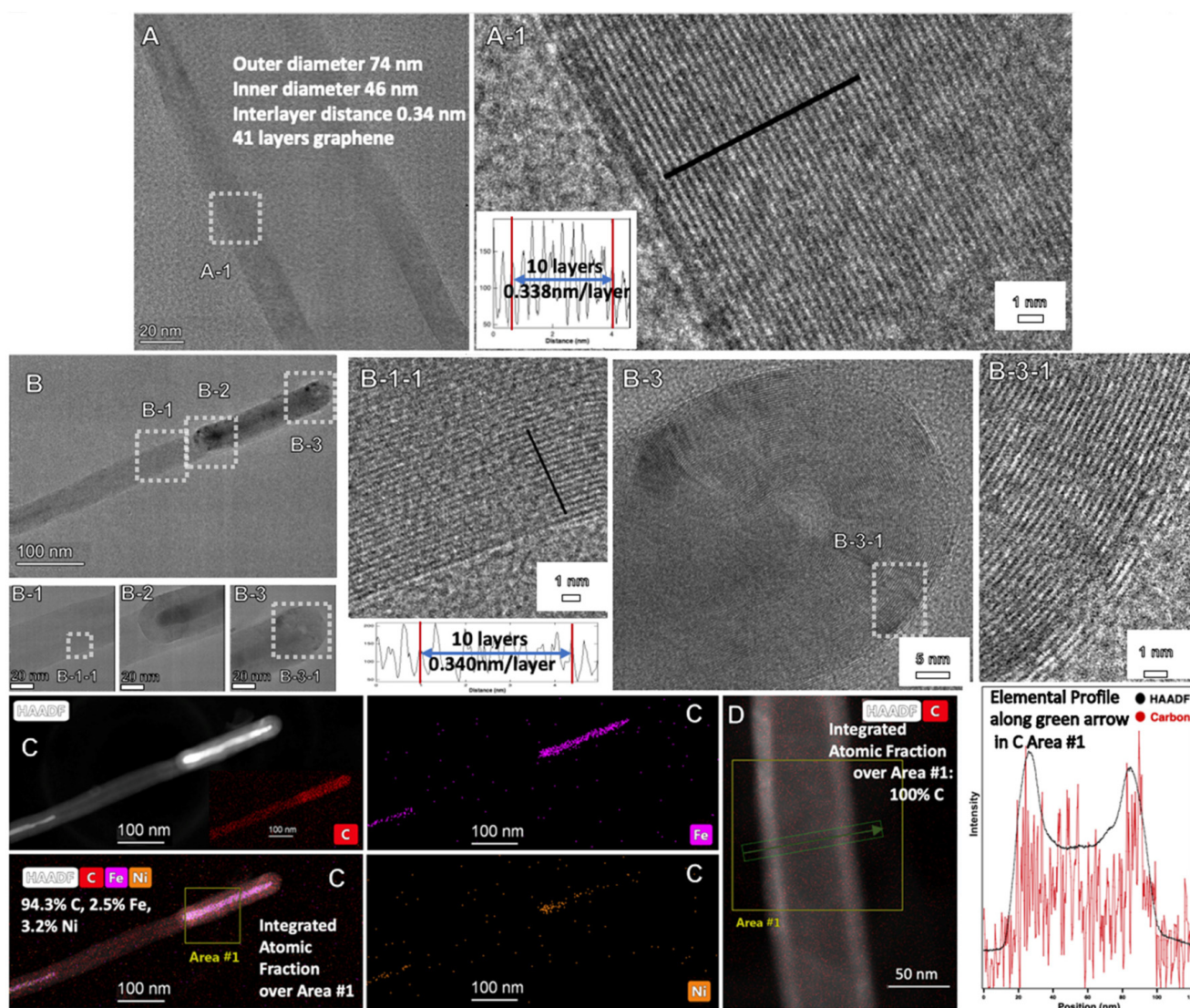

Figure 3. TEM and HAADF of the synthesis product of high-purity, high-yield carbon nanotubes under the Electrolysis E (Table 1) electrochemical conditions by electrolytic splitting of CO_2 in 770 °C Li_2CO_3. In the top row, the product is analyzed by TEM with scale bars of 20 nm (left panel) or 1 nm (right). Moving left to right in the second row, there are scale bars of 100, 5, 5, and 1 nm. The third row's scale bars are 100 or 50 nm. The bottom row scale bars are 20, 1, and 1 nm. Panels: (**A,B**), B-1, B-2, B-3, B-3-1 TEM; A-1, B-1-1 TEM, with measured graphene layer thickness. (**C**): Elemental HAADF elemental analysis; (**D**): HAADF element analysis with (right side) elemental profile.

In Figure 3 on the right side of row 2, the parallel 0.34 nm spacing for the graphene layers in the CNT walls is again observable. This panel also includes dark areas of metal

trapped within the CNT, and serves as a snapshot in time of the growth of the CNT. In the third row of the figure, it can be seen that HAADF analysis of Area 1 revealed an elemental composition for this area, including the walls with the trapped interior metal, of 94.4% carbon, 2.5% Fe, and 3.2% Ni, as distributed according to the individual C, Fe, and Ni HAADF maps included in the figure. The second row of the figure also shows the tip of the CNT, which included trapped metal. The transition metal served as a nucleating agent, which supported the formation of the curved graphene layers shown at the tip of the CNT, which is a major component of the CNT growth mechanism. While occurring in an entirely different physical chemical environment than chemical vapor deposition (CVD), this molten carbonate electrolysis process of transition metal nucleated growth of CNTs appeared to be similar to those noted to occur for CVD CNT growth. This was the case despite the fact that CVD is a chemical/rather than electrochemical process, and occurs at the gas/solid, rather than liquid/solid interface.

2.3. Tailored Electrochemical Growth Conditions Producing High-Aspect-Ratio CNTs from CO_2

Figure 4 presents the product's SEM of the electrochemical configuration that yielded the longest (100 to 500 μm long) and highest purity (98%) CNTs at high coulombic efficiency (99.5%) of those studied here (described as Electrolysis F in Table 1). As with the previous configuration that yielded nearly as high-purity, but shorter, CNTs. The synthesis used an 0.1 wt% Fe_2O_3 additive to the Li_2CO_3 electrolyte, a Muntz Brass cathode, and an Inconel 718 anode with a layered Inconel 600 screen. However, this synthesis found an optimization in CNT purity and length using two, rather than three layers of Inconel 600, and using a higher current density (0.4, rather than 0.08, A/cm^2) and shorter electrolysis time (4, rather than 15, hours). With a diameter of <0.2 μm, these CNTs could have an aspect ratio of >1000. As correlated with the alloy composition in Table 1, the smaller number of Inconel 600 layers reflected the need for the inclusion of anodic molybdenum available in that alloy, but at a controlled, lower concentration, to achieve the resultant high-purity, high-aspect-ratio CNTs. As seen in the figure, the CNTs were densely packed and largely parallel, and as discussed in sect. 2.5, would be a useful candidate for use in nano-filtration.

Figure 5 presents TEM and HAADF probes of the high-aspect-ratio CNT product of Electrolysis F (as described in Table 1, and by SEM in Figure 4). As seen on the right side of the middle row of the figure, the CNT walls consisted of parallel carbon (layers separated by the characteristic 0.33–0.24 nm graphene layer spacing). As seen in the elemental analysis of Area 1 in the lowest row, the areas consisted of hollow tubes composed of 100% carbon. However, as seen in the TEM of the top two rows and in the bottom row as the HAADF elemental profiles, there were also extensive portions of the tubes that were intermittently filled with metal. In the bottom row of the figure, a lateral cross sectional elemental CNT profile scanned through Area 2 from the outside, through the CNT and then out the opposite wall, shows that the wall was composed of carbon, while the inner region also contained iron as the dominant metal coexisting with some nickel.

2.4. Tailored Electrochemical Growth Conditions Producing Thinner CNTs from CO_2

Figure 6 demonstrates additional electrochemical conditions that yielded high-purity carbon nanotubes by CO_2 molten electrolysis. In the top row, panels H, as with high current density (Figure 2 panels A), a moderate current density of 0.4 A/cm^2 (with the same electrolyte, a Muntz Brass cathode and a Nichrome C anode) yielded high-purity (96%) CNTs that were somewhat longer (100–200 μm) at a coulombic efficiency approaching 100%. Switching the cathode material to Monel, as shown in the second row (Figure 6, panels a), yielded shorter 20–50 μm CNTs with 97% purity and coulombic efficiency again approaching 100%. Not shown in the figure, but included in Table 1 (Electrolysis D), is the fact that a switch from Nichrome C to a pure nickel anode (while retaining the Monel Cathode, and with electrolyte additives at J = 0.2 A/cm^2) led to a substantial drop in CNT purity to 70% with the remainder of the product consisting of nano-onions. A drop of current density from 0.4 A to 0.1 A/cm^2, as shown in in Figure 6 panels K, yielded 97%

purity CNTs of 30–60 μm length with only a small drop of coulombic efficiency to 97%. In a single panel of L located in the lower left corner of Figure 6, it can be seen that an overabundance of Fe_2O_3 was added, which was previously observed to lead to a loss of control of the synthesis specificity [45]. In this case, the total purity of the CNTs remained high at ~95%, but this consisted of two distinct morphologies of CNT in the product. The majority product, at ~75%, was twisted CNTs, and the minority product, at ~20%, was straight CNTs. Finally, in panels M on the middle and right lowest row of Figure 6, a noble metal, iridium, was used as the anode (along with the Monel Cathode) at a low 0.08 A/cm^2 current density. Transition metals released from the anode, during its formation of a stable oxide over layer, can contribute to the transition metals ions that are reduced at the cathode and serve as nucleation points for the CNTs. This was not the case here due to the high stability of the iridium. Instead, as a single, high concentration transition metal, 0.81 wt% Cr was made as the electrolyte additive. The product was highly pure (97%) CNTs that were the thinnest shown (<50 nm diameter), were 50–100 μm long for an aspect ratio > 1000, and formed at a coulombic efficiency of 80%.
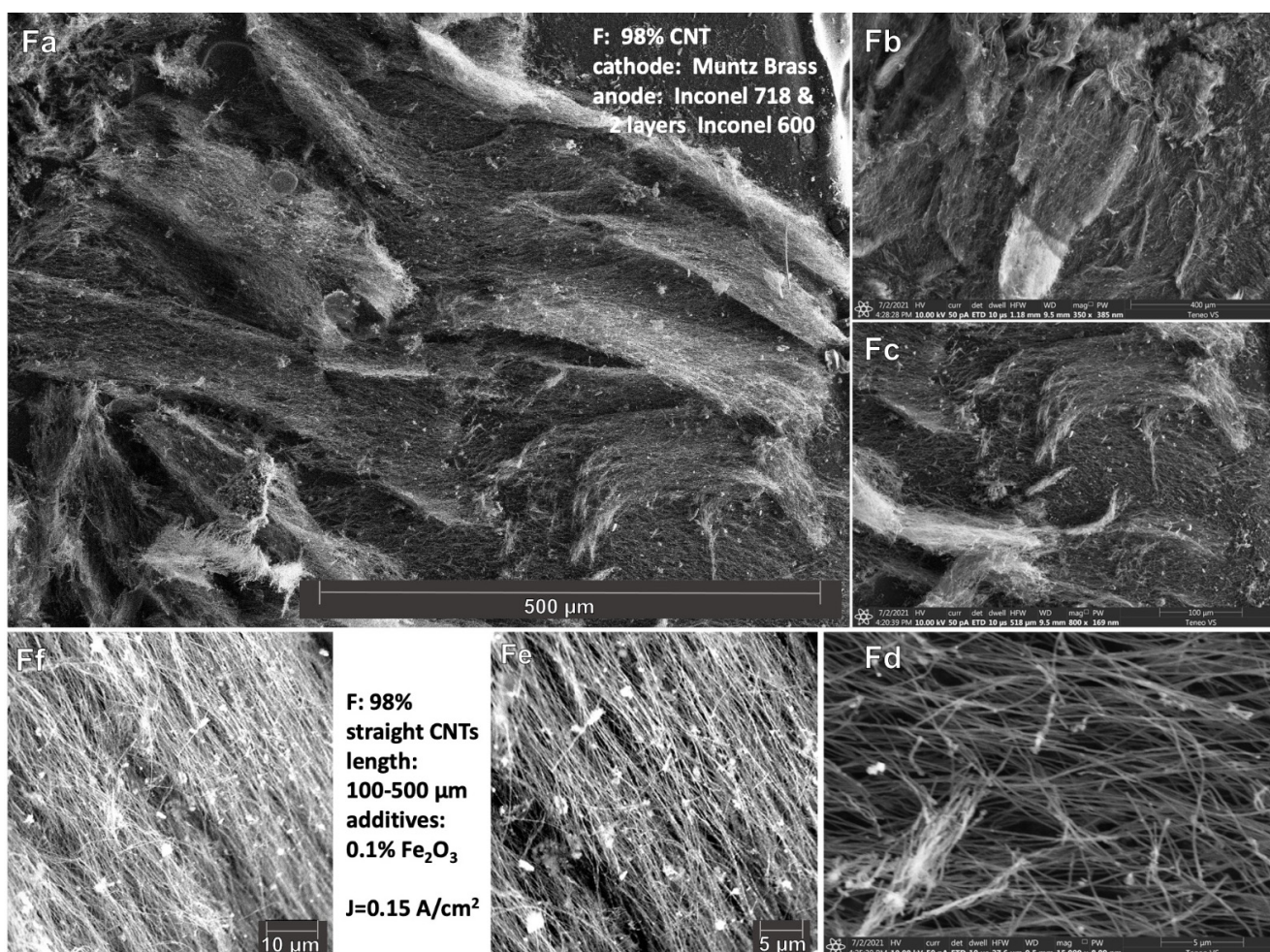

Figure 4. SEM of the synthesis product of high-aspect-ratio (and high-purity and high-yield) carbon nanotubes prepared by electrolysis F in Table 1, splitting CO_2 in 770 °C Li_2CO_3. Moving left to right in the panels, the product is analyzed by SEM with increasing magnification. Scale bars in panels Fa-Ff (clockwise from top) are 500, 400, 100, 5, 5, and 10 μm.
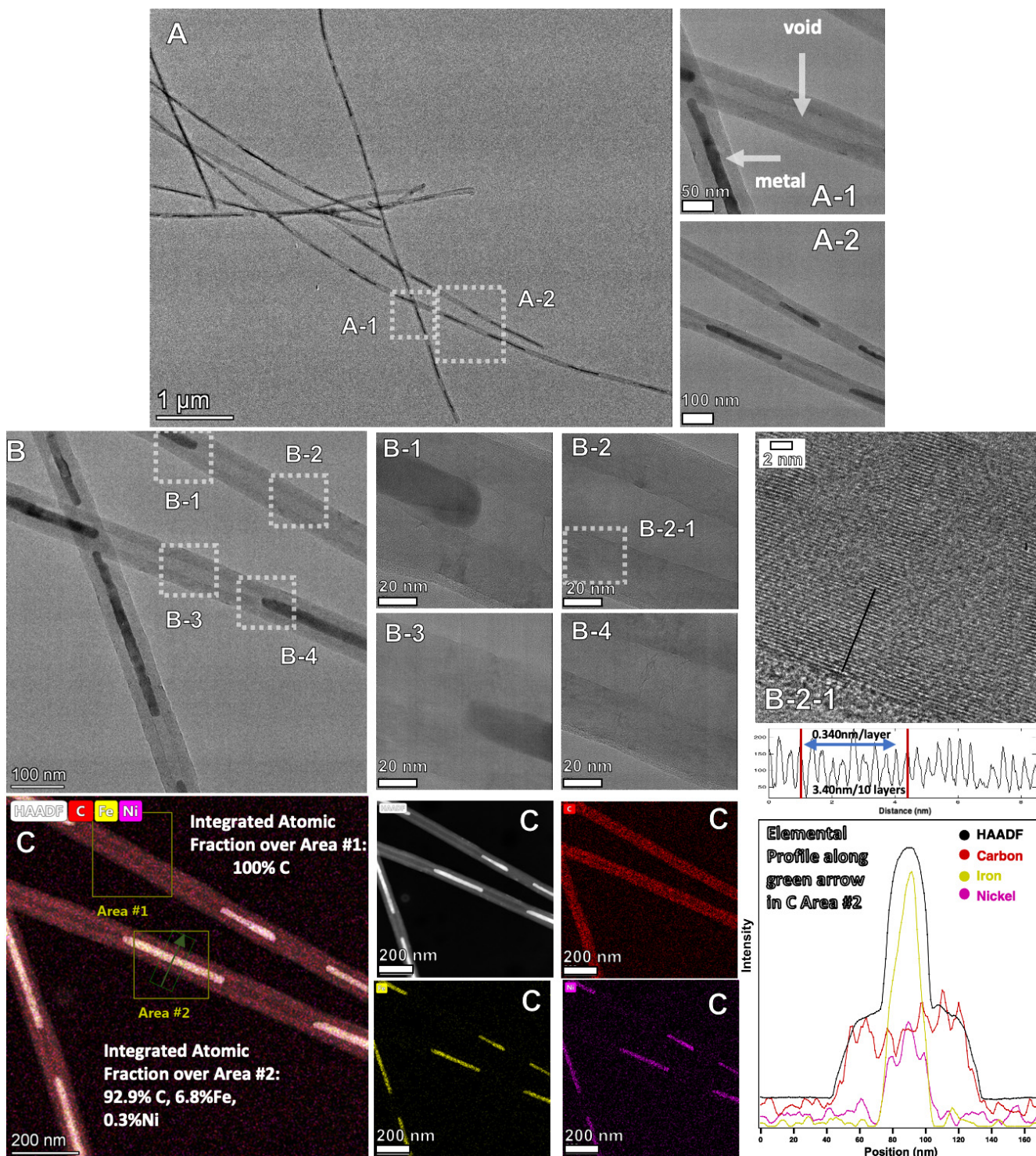
Figure 5. TEM and HAADF of the synthesis product of high-purity, high-yield carbon nanotubes under the Electrolysis F (Table 1) electrochemical conditions by electrolytic splitting of CO_2 in 770 °C Li_2CO_3. In the top row, the product is analyzed by TEM with scale bars of 1 μm (left panel) or 100 nm (right). Scale bars in the middle right moving left to right are of 50, 20, and 1 nm. HAADF measurements in the bottom panel each have scale bars of 200 nm. Panels: (**A**), A-1, A-2, (**B**), B-1, B-2, B-3, B-4: TEM; B-2-1 TEM with measured graphene layer thickness. (**C**): Elemental HAADF elemental analysis with (right side) elemental profile.
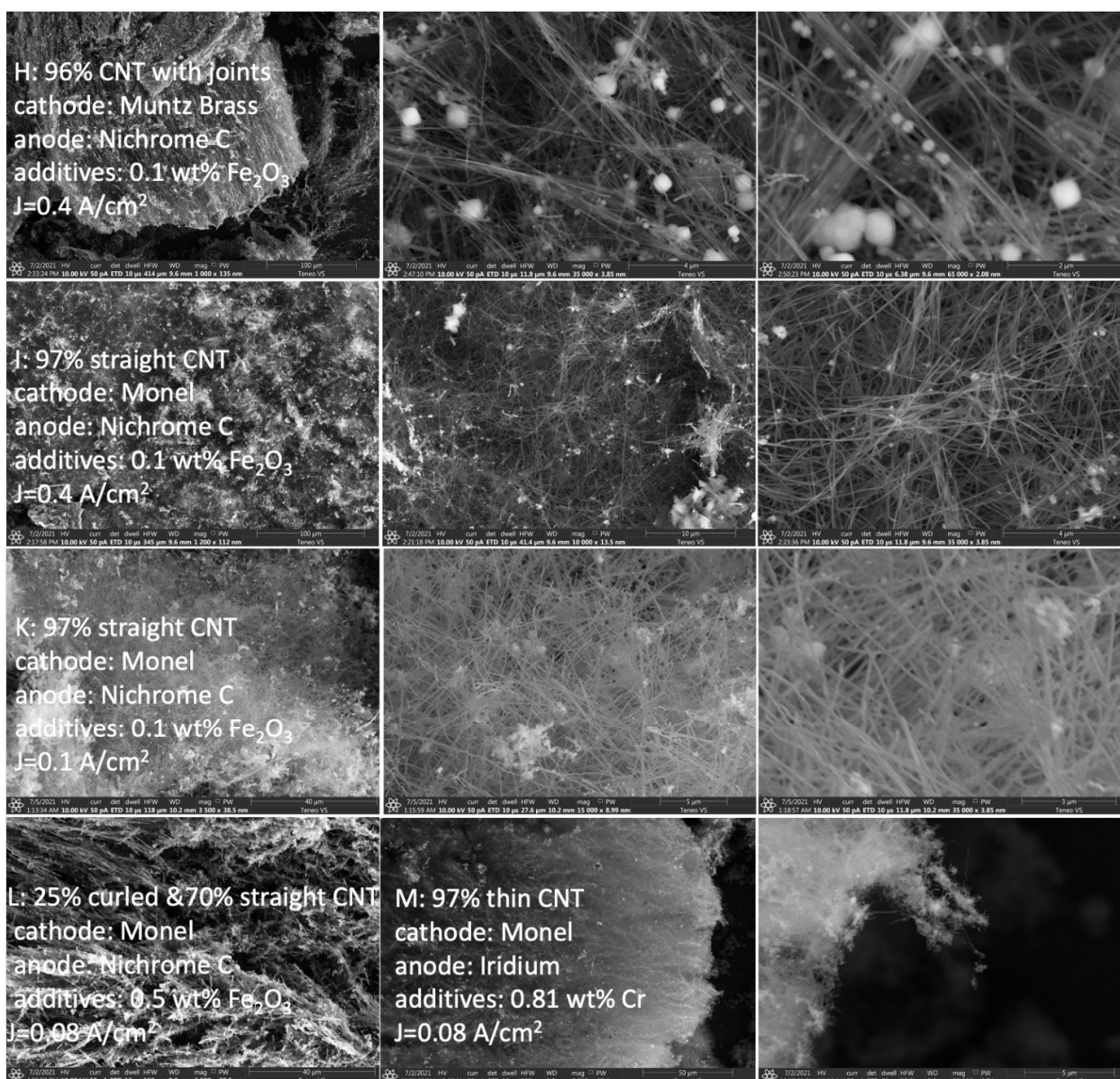
Figure 6. SEM of the synthesis product of high-purity, high-yield carbon nanotubes under a variety of electrochemical conditions by electrolytic splitting of CO_2 in 770 °C Li_2CO_3. The washed product was collected from the cathode subsequent to the electrolysis described in Table 1. Scale bars (starting from left) are for panels H: 100, 4, and 2 μm; for panels I: 100, 10, and 4 μm; for panels K: 40, 5, and 3 μm; for panels L: 40, 50, and 5 μm.

SEM analysis of several of the synthesis products, specifically Electrolyses H, B, and C, revealed evidence of nodules that appeared as "buds" attached to the CNTs. These buds were the most consistent in Electrolysis H and were explored by TEM and HAADF, as shown in Figure 7. It is fascinating, as seen in the top row of the figure, that the buds generally had a spherical symmetry, and while not prevalent in the structure, appeared in a structure comparable to grape bunches growing on a vine. The buds generally contained a low level of the transition metal nucleating metal, such as the 0.3% Fe shown, and the rest of the structure was generally pure carbon, with an occasional metal core. This low level of metal used was easily removed by an acid wash. Previously introduced higher levels of Ni or Fe could lead to magnetic carbon nanotubes with useful properties of recyclability, filtration, and shape-shifting materials among other applications [41]. As seen in the left side of the second row, the carbon nanotube walls continued to exhibit the regular 0.33 to

0.34 graphene interwall separation, as seen on the right side of the row, and the adjacent CNTs may have had merged or distinct graphene structures. Similarly, as seen in the third row of Figure 2, the adjacent buds on the CNTs could have graphene walls that bended to join, and were shared, or, as seen in the fourth row, appeared instead to be distinct (intertwined, not merged) structures.
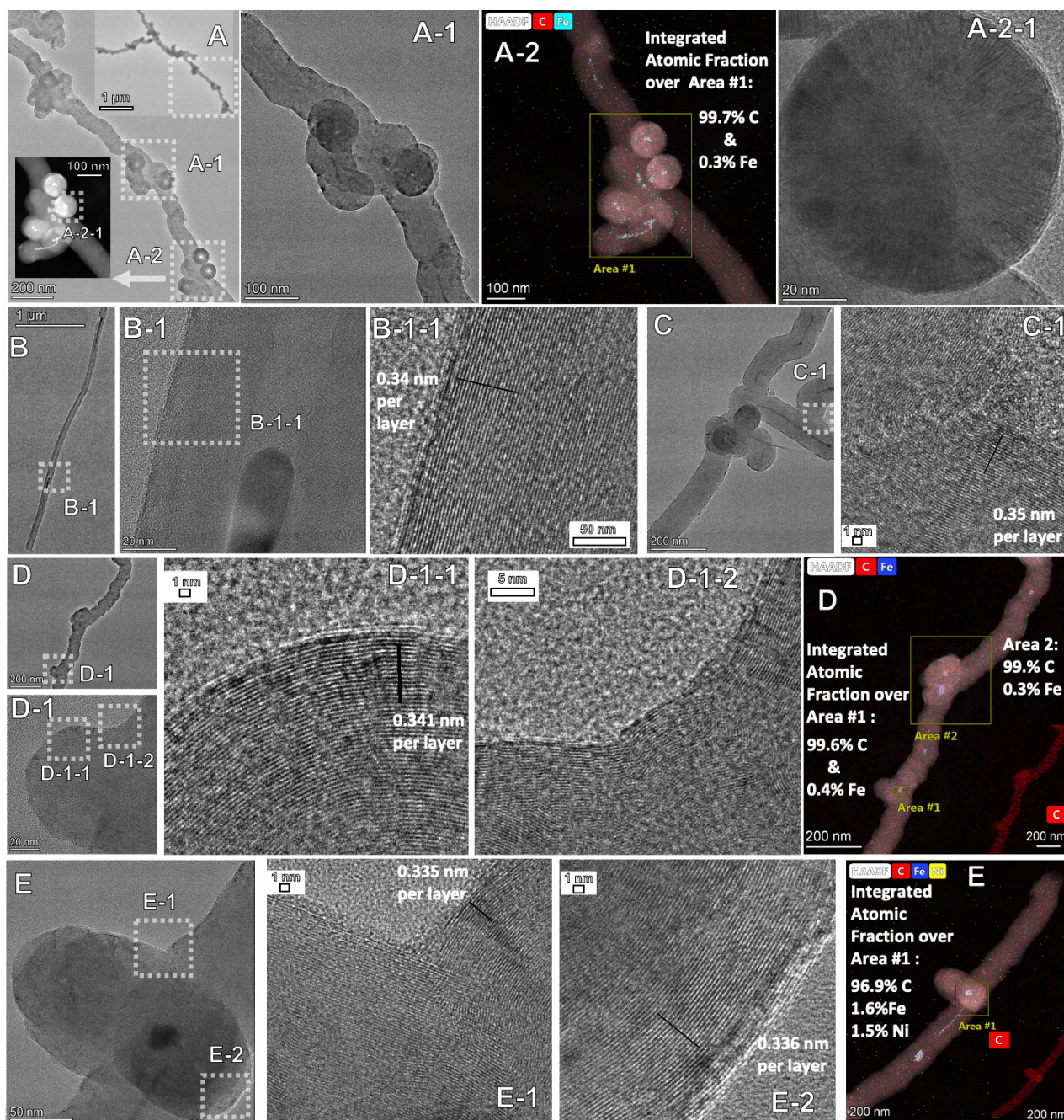

Figure 7. TEM and HAADF of the synthesis product of carbon nanotubes that exhibited nodules or buds under the Electrolysis H (Table 1 and SEM on top row of Figure 6) electrochemical conditions by electrolytic splitting of CO_2 in 770 °C Li_2CO_3. In the top row, the product is analyzed with scale bars from left to right of 200, 100, 20 and 100 nm. Scale bars in the second right row are of 1μm, then 20, 5, 200, and 1 nm. The third row scale bars are 200, 20, 1, 5, and 200 nm. The bottom row scale bars are 50, 1, 1, and 200 nm. TEM Panels: (**A**) A-1, A-2-1, (**B**), B-1, B-1-1, (**C**), C-1, C-2, D-1-1, D-1-2, (**E**), E-1, E2: TEM; A-2, (**D**,**E**) also include Elemental HAADF elemental analyses.

2.5. Electrochemical Conditions to Synthesize Macroscopic Assemblies of CNTs

In addition to individual CNTs, the final series of electrolyses generated useful macroscopic assemblies of CNTs. There has been interest in densely packed CNTs for nanofiltration, and also, due to their high density of conductive wires, as an artificial neural net [52–62]. CNTs' aerogels have been reported as being formed by CVD and/or also reported as being formed within molds. Their sorbent properties have been investigated for applications such as the cleanup of chemical leakages under harsh conditions. Those studies noted that such aerogel matrices, consisting of highly porous, intermingled CNTs, can be repeatedly compressed to a small fraction of their initial volume without damaging the structure of the carbon nanomaterials [52–56].

The term "Nanofiltration" was proposed in 1984 to solve the terminology problem for a selective reverse osmosis process that allows ionic solutes in a feed water to permeate through a membrane [57]. In addition to low energy consumption, with respect to alternative unit operations such as distillation and evaporation, thermal damage of heat-sensitive molecules can be minimized during the separation due to the potential for low operating temperatures of nanofiltration [58]. Small-diameter CNTs were demonstrated due to their ability to be used as a nanofiltration or molecular sieve to selectively remove larger size molecules from smaller size molecules, such as the selective removal of cyclohexane from n-hexane [57]. There is a need to control the fabrication of macroscopic assemblies of CNTs to optimize their capabilities for nanofiltration, and CNT assemblies synthesized by CVD and laser ablation have been investigated [52–56,58–61].

An artificial neural network is a collection of interconnected nodes that loosely model the neurons in a biological brain. Estimates of biologic neuronal density (rat) are in the range of 100 in a 100 μm cube (10^5/mm^3) on each side. The fabrication of an artificial neural network with a structure that mimics that number of nanowires and nodes presents a challenge. However, this is in the same size domain as macroscopic assemblies of CNTs. For example, Gabay and co-workers explored the engineered self-organization of neural networks using carbon nanotube clusters [38], emphasizing the need for improved pathways to fabricate and control macroscopic assemblies of CNTs.

The macroscopic assemblies observed in this study are referred to as nano-sponge, densely packed parallel CNTs, and nano-web CNTs, in Table 3 and Figure 8. The Nano-sponge assembly was formed by Electrolyses N with Nichrome C serving as both the cathode and the anode, with 0.81% Ni powder added to the 770 °C Li$_2$CO$_3$ electrolyte, the initial current ramped upwards (5 min each at 0.008, 0.016, 0.033 and 0.067 A/cm^2), then a 4h current density of 0.2 A/cm^2 generating a 97% purity nanosponge at 99% coulombic efficiency. As previously described, long, densely packed, parallel carbon nanotubes were produced in Electrolysis F with a 0.1 wt% Fe$_2$O$_3$ additive to the Li$_2$CO$_3$ electrolyte, a Muntz Brass cathode and an Inconel 718 anode, and two layers of Inconel 600 screen at 0.15 A/cm^2.

Table 3. Systematic variation of CO$_2$ splitting conditions in 770 °C Li$_2$CO$_3$ to optimize the formation of macroscopic assemblies of nanocarbons with densely packed carbon nanotubes.

| Electrolysis	Cathode	Anode	Additives (wt% Powder)	Electrolysis Time	Current Density (A/cm^2)	Product Description
N	Nichrome C	Nichrome C	0.81% Ni	4 h	0.2	97% nano-sponge CNT
F	Muntz Brass	Inconel 718 2 layers Inconel 600	0.1% Fe$_2$O$_3$	4 h	0.15	98% dense packed straight 100–500 μm CNT
P	Muntz Brass	Nichrome C 3 layers Inconel 600	0.1% Fe$_2$O$_3$	15 h	0.08	97% 50–100 μm nano-web CNT
Q	Monel	Nichrome C	0.81% Ni	3 h	0.2	92% 5–30 μm nano-web CNT Rest: onions
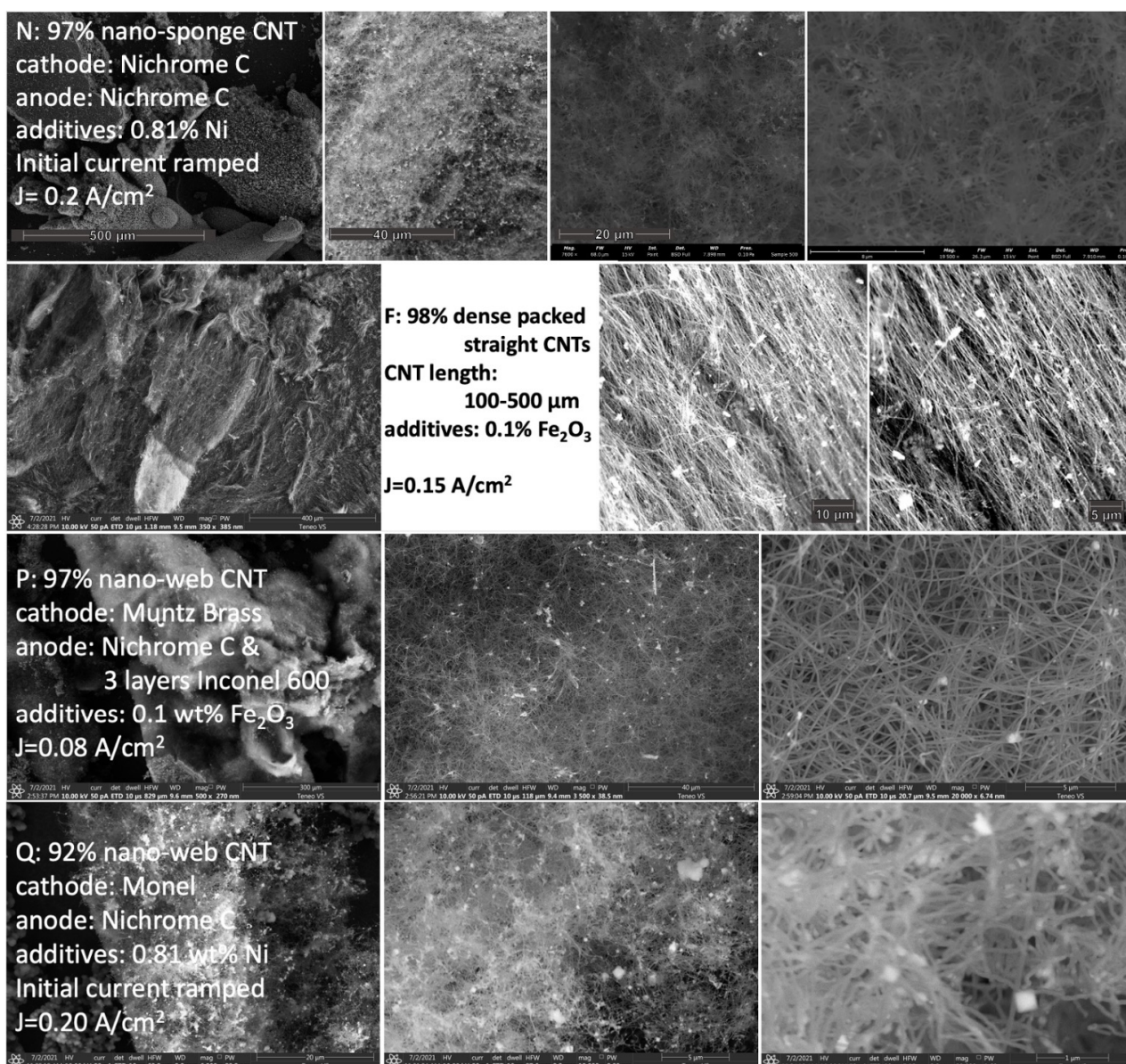
Figure 8. SEM of the synthesis product consisting of carbon nanotubes arranged in various packed macroscopic structures that are amenable to nano-filtration. The washed product was collected from the cathode subsequent to the electrolysis described in Table 3. Moving from left to right in the panels, the product is analyzed by SEM with increasing magnification. Scale bars in panels These include nano-sponge, dense packed straight, and nano-web CNTs. Moving from left to right in the panels, product is analyzed by SEM in the top two rows (N), and subsequent rows P and Q, with increasing magnification. Scale bars in panels (starting from left) are for top panels N: 500, 40, 20, and 8 μm; for lower panels N: 400, 10, and 5 μm; for panels P: 300, 40, and 5 μm; for panels Q: 500, 40, 20, and 8 μm.

As opposed to the parallel assembly produced in Electrolysis F, nano-web aptly describes the interwoven carbon nanotubes from Electrolyses P and Q, presented in the lower rows of Table 3 and Figure 8. Two different routes to the nano-web assembly are summarized. The first uses an 0.1% Fe_2O_3 additive, a Muntz Brass cathode, and an Inconel 718 anode with three layers of Inconel 600 screen, at 0.08 A/cm^2, generating a nano-web with a purity of 97% at a coulombic efficiency of 79%. The second pathway uses an 0.81% Ni powder additive, a Monel cathode, and Nichrome C anode, at 0.28 A/cm^2, generating a nano-web with a purity of 92% at a coulombic efficiency of 93%.

The densely packed straight CNTs had an inter-CNT spacing ranging from 50 to 300 nm; moreover, the CNTs were highly aligned, providing unusual nanofiltration opportunities for both this size domain, and for an opportunity to filter 1D from 3D morphologies. The nano sponge did not have this alignment feature, and as shown in Figure 8, provided nanofiltration pore sizes of 100 to 500 nm, while the nano-web product provided nanofiltration with pore sizes of 200 nm to 1 μm. Future studies will investigate the effectiveness of this portfolio of macroscopic CNT assemblies for nanofiltration.

2.6. Raman and XRD Characterization of the CNTs and Their Macro-Assemblies

Figure 9 presents the Raman spectra effect of variation of the CNT electrolysis conditions on the CNT assembly products from CO_2 electrolysis in 770 °C Li_2CO_3. The Raman spectrum exhibits two sharp peaks ~1350 and ~1580 cm^{-1}, which correspond to the disorder-induced mode (D band) and the high-frequency E_{2G} first order mode (G band), respectively, and an additional peak, the 2D band, at 2700 cm^{-1}. In the spectra, the graphitic fingerprints lie in the 1880–2300 cm^{-1} and are related to different collective vibrations of sp-hybridized C-C bonds.

Table 4. Raman spectra of a diverse range of carbon allotropes and macro-assemblies formed by molten electrolysis.

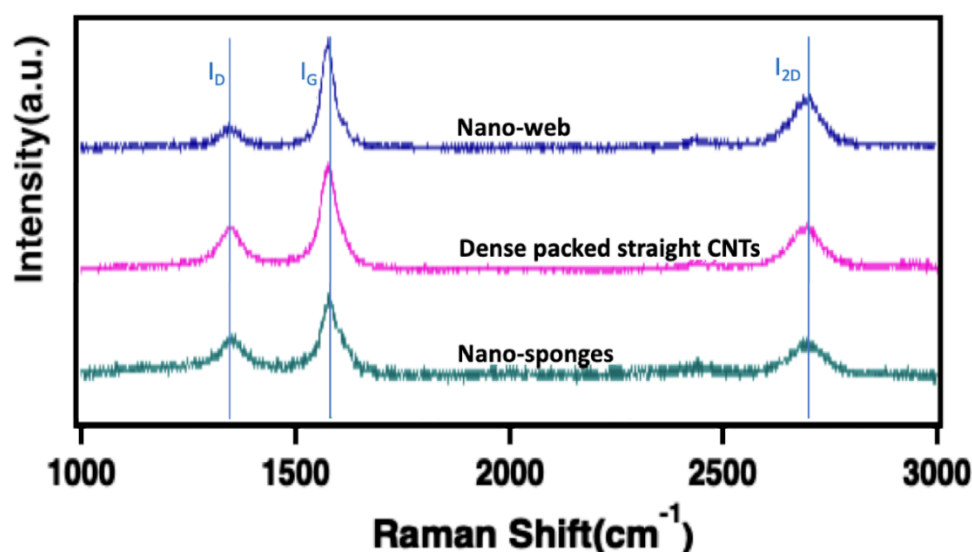| CO_2 Molten Electrolysis Product Description	ν_D (cm^{-1})	ν_G (cm^{-1})	ν_{2D} (cm^{-1})	I_D/I_G	I_{2D}/I_G
Nano-web	1342.5	1577	2689.6	0.28	0.50
Dense packed CNTs	1342.5	1577.4	2694.8	0.46	0.49
Nano-sponge	1352.5	1580.6	2687.3	0.67	0.62

Figure 9. Raman spectra of the synthesis product consisting of various labeled carbon nanotube assemblies synthesized by the electrolytic splitting of CO_2 in 770 °C Li_2CO_3 with a variety of systematically varied electrochemical conditions described in Table 4.

Interpretation of the Raman spectra provides insights into the potential applications of the various carbon allotropes. As shown in Figure 9, the intensity ratio between the D band and the G band (I_D/I_G) was calculated; this ratio, and the observed shift in the I_G frequency, are useful parameters to evaluate the relative number of defects and degree of graphitization, and are presented in Table 4. Note in particular that, of the nano-sponge, nano-web, and densely packed CNT assemblies described in Figure 8 and Table 3, the nano-web CNT assembly exhibited low disorder, with $I_D/I_G = 0.36$, as shown in Table 4, the densely packed CNT assembly exhibited intermediate disorder with $I_D/I_G = 0.49$, and

the nano-sponge exhibited the highest disorder with I_D/I_G = 0.62 while accompanied by a shift in I_G frequency.

That is, for the assemblies with increasing I_D/I_G ratio: CNT nano-web < Dense packed CNT < CNT nano-sponge.

Previously, increased concentrations of iron oxide added to the Li_2CO_3 electrolyte were correlated with an increasing degree of disorder in the graphitic structure [38]. It should be noted that these defect levels each remain relatively low as the literature is replete with reports of multiwalled carbon nanotubes made by other synthetic processes with I_D/I_G > 1. Lower defects are associated with applications that require high electrical power and strength, while high defects are associated with applications that permit high diffusivity through the structure, such as those associated with increased intercalation and higher anodic capacity in Li-ion batteries and higher charge supercapacitors.

Along with the XRD library of relevant compound spectra, XRD results of the CNT assembly products are presented in Figure 10, prepared as described in Figure 8 and Table 3. Each of the spectra exhibited strong diffraction peaks at 2θ = 27°, characteristic of graphitic structures. The nano-sponge XRD spectra was distinct from the others, with a dominant peak at 2θ = 43°, indicating the presence of iron as $Li_2Ni_8O_{10}$ and chromium as $LiCrO_2$ by XRD spectra match. The XRD result of this nano-sponge exhibited little or no iron carbide. On the other hand, both the nano-web and densely packed straight CNTs exhibited additional significant peaks at 2θ = 42 and 44°, indicative of the presence of iron carbide, Fe_3C. The diminished presence of defects previously noted by the Raman spectra for the other densely packed CNTs, along with the XRD presence of $Li_2Ni_8O_{10}$, $LiCrO_2$, and Fe_3C, provide evidence that the co-presence of Ni, Cr, and Fe as nucleating agents can diminish defects in the CNT structure compared to Ni and Cr alone.
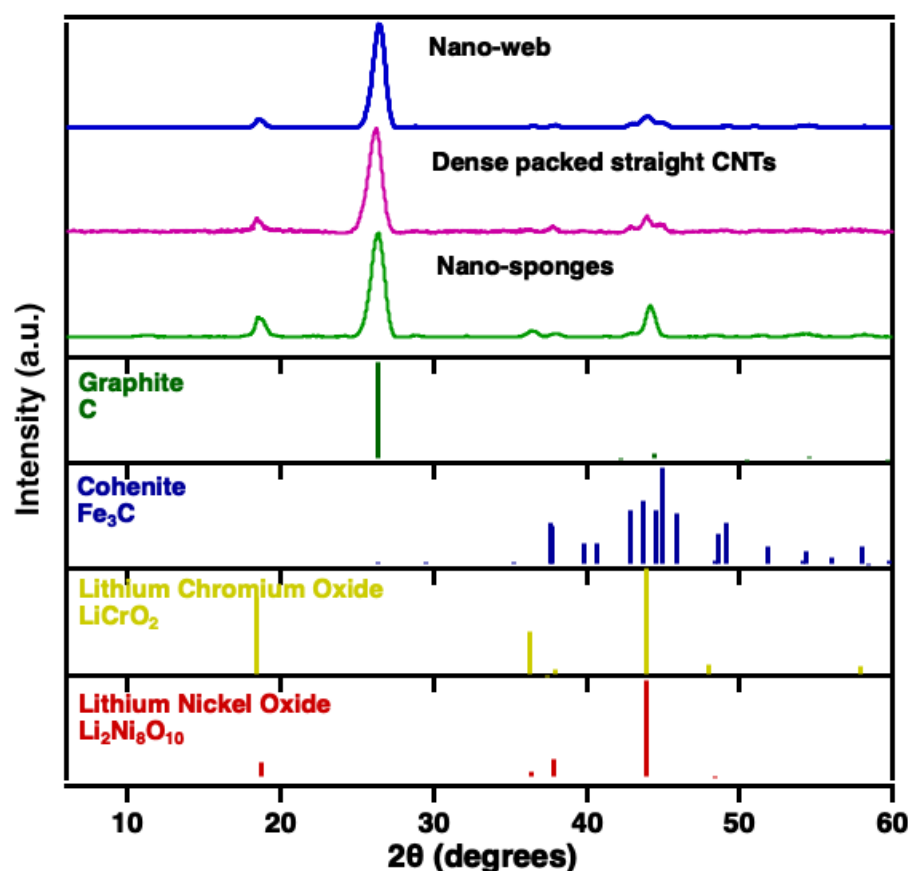

Figure 10. XRD of the synthesis product consisting of various labeled carbon nanotube assemblies synthesized by the electrolytic splitting of CO_2 in 770 °C Li_2CO_3 with a variety of systematically varied electrochemical conditions described in Table 4.

3. Materials and Methods

3.1. Materials

Lithium carbonate (Li_2CO_3, 99.5%), lithium oxide (Li_2O, 99.5%), lithium phosphate Li_3PO_4 (Li_3PO_4, 99.5%), iron oxide (Fe_2O_3, 99.9%, Alfa Aesar), and boric acid (H_3BO_3, Alfa Aesar 99+%) were used as electrolyte components in this study. For electrodes, Nichrome A (0.04-inch-thick), Nichrome C (0.04-inch-thick), Inconel 600 (0.25-in thick), Inconel 625 (0.25-in thick), Monel 400, Stainless Steel 304 (0.25-in thick), Muntz Brass (0.25-in thick), were purchased from onlinemetals.com (accessed on 14 December 2021). Ni powder was 3–7 μm (99.9%, Alfa Aesar). Cr powder was <10 μm (99.2%, Alfa Aesar). Co powder was 1.6 μm (99.8%, Alfa Aesar). Iron oxide was 99.9% Fe_2O_3 (Alfa Aesar). Co powder was 1.6 μm (99.8%, Alfa Aesar). Inconel 600 (100 mesh) was purchased from Cleveland Cloth. The electrolysis was a conducted in a high form crucible >99.6% alumina (Advalue).

3.2. Electrolysis and Purification

Specific electrolyte compositions of each electrolyte are described in the text. The electrolyte was pre-mixed by weight in the noted ratios then metal or metal oxide additives were added if used. The cathode was mounted vertically across from the anode and immersed in the electrolyte. Generally, the electrodes were immersed subsequent to electrolyte melting. For several noted electrolyses, once melted, the electrolyte was maintained at 770 °C ("aging" the electrolyte) prior to immersion of the electrolytes, followed by immediate electrolysis. Generally, the electrolysis was driven with a described constant current density. As noted, for some electrolyses, the current density was ramped in several steps building to the applied electrolysis current, which was then maintained at a constant current density. Instead, most of the electrolyses were initiated, and held, at a single constant current. The electrolysis temperature was 770 °C using CO_2 directly from the air. In the C2CNT process, the electrolytic splitting can occur as direct air carbon capture without CO_2 pre-concentration [31–34,36–44,47–51], or with concentrated CO_2, or CO_2 exhaust gas including during the scaling up of this process, in which the CO_2 transformation to CNTs was awarded the 2021 Carbon XPrize XFactor award for producing the most valuable product from CO_2 [32,45,46,62–64]. In this study, as the electrolysis cell directly captured CO_2 from the air via Equation (1), no additional introduction of CO_2 was needed. A simple measure of sufficient CO_2 uptake is whether the electrolyte level falls during the course of the electrolyte. As mentioned, the ^{13}C isotope of CO_2 was previously used to track carbon through the C2CNT process from its origin (CO_2 as a gas phase reactant) through its transformation to a CNT or carbon nanofiber product, and the CO_2 originating from the gas phase served as the renewable C building blocks in the observed CNT product [32]. If CO_2 uptake was insufficient, then the carbonate electrolyte was instead consumed in accord Equation (2), rather than renewed in accord with Equations (1) and (2) in tandem. For example, when conducting at high electrolysis rates of 1 A/cm^2 or greater (not the situation of this study), then gas containing CO_2 needed to be bubbled into the electrolyte, otherwise the electrolyte was consumed and the level of electrolyte visibly fell [40].

3.3. Product Characterization

The raw product was collected from the cathode after the experiment and cool down, followed by an aqueous wash procedure that removed electrolyte congealed with the product as the cathode cooled. The washed carbon product was separated by vacuum filtration. The washed carbon product was dried overnight in a 60 °C oven, yielding a black powder product.

The coulombic efficiency of electrolysis is the percent of applied, constant current charge that was converted to carbon, determined as:

$$100\% \times C_{experimental}/C_{theoretical} \tag{4}$$

This was measured by the mass of washed carbon product removed from the cathode, $C_{experimental}$, and calculated from the theoretical mass, $C_{theoretical} = (Q/nF) \times (12.01\,\text{g C mol}^{-1})$, which was determined from Q, the time-integrated charged passed during the electrolysis, F, the Faraday (96485 As mol^{-1} e^{-}), and the n = 4 e^{-} mol^{-1} reduction of tetravalent carbon, consistent with Equation (2).

Characterization: The carbon product was washed, and analyzed by PHENOM Pro Pro-X SEM (with EDX), FEI Teneo LV SEM, and by FEI Teneo Talos F200X TEM (with EDX). XRD powder diffraction analyses were conducted with a Rigaku D = Max 2200 XRD diffractometer and analyzed with the Jade software package. Raman spectra were collected with a LabRAM HR800 Raman microscope (HORIBA). This Raman spectrometer/microscope used an incident laser light with a high resolution of 0.6 cm^{-1} at 532.14 nm wavelength.

4. Conclusions

Molten carbonate electrolysis of CO_2 provides an effective path for the C2CNT synthesis of CNTs and macroscopic CNT assemblies. This study explored a variety of electrochemical configurations, systematically varying the electrode composition, electrode current density, electrolysis time, current ramping initiation, and electrolyte additives and their concentrations. The highest observed CNT purity synthesis (97%) utilized a specialized anode consisting of two layers of high-surface-area Inconel 600 (screen) on Inconel 718, a Muntz Brass cathode, with an 0.1 wt% Fe_2CO_3 additive to the 770 °C Li_2CO_3 electrolyte, and with the electrolysis current conducted for 4 h at an intermediate current density (without current ramping) of 0.15 mA/cm^2. The product, as analyzed by SEM, was aligned CNTs with a length of 100 to 500 μm and an aspect ratio of over 1000. The anode, cathode, and electrolyte additive choice were found to be effective for controlling the transition metal nucleation, which is critical to high-purity electrolytic CNT growth.

In a sister paper [51], slight variations of the synthesis parameters led to the formation of a variety of new, high-purity, non-CNT nanocarbon allotropes. All syntheses in the present study produced a majority of CNTs, but the morphology of the CNT product changed widely with the synthesis conditions. Depending on the synthesis conditions, alternate CNT products that were as short as 10 to 30 μm, and curled, rather than straight, or mixed with carbon nano-onions were observed. The high-purity product exhibited a sharp XRD graphic peak, and a low Raman I_D/I_G ratio, which was indicative of low defects in the carbon structure. The XRD also contained iron carbide, and nickel and chromium lithium oxides, which, based on TEM, were found to be located within the CNT.

TEM HAADF showed that the inner core of the CNT length was generally free of metals (void, with 100% carbon walls), but in other areas, the void was filled with transition metal. As they were produced by molten carbonate electrolysis, the CNT walls were conclusively shown to be comprised of highly uniform concentric, cylindrical graphene layers with graphene characteristics and inter-layer spacing of 0.33 to 0.34 nm. When the internal transition metal was within the CNT tip, the layered CNT graphene walls were observed to bend in a highly spherical fashion around the metal supporting the transition metal nucleated CNT growth mechanism. Several syntheses had unusual nodules, many of them highly spherical, on the CNT, generally comprising carbon and containing a low level of internal transition metal. Generally, intersecting CNTs did not merge, but in a few cases, graphene layers bent to become part of the CNT intersection, which was consistent with the occurrence of the occasional, related growth of intersecting CNTs, such as branching.

The study also demonstrates new syntheses of assemblies of CNTs by means of the C2CNT process, with structural implications towards their potential applications for nanofiltration and neural nets and demonstrated pores sizes ranging from 50 nm to 1 μm.

Author Contributions: Conceptualization, S.L. and G.L.; methodology, S.L., X.L., G.L. and X.W.; writing S.L. and G.L. All authors have read and agreed to the published version of the manuscript.

Data Availability Statement: The authors confirm that the data supporting the findings of this study are available within the article.

Conflicts of Interest: The authors declare no conflict of interest.

References

1.　CO$_2$-Earth: Daily CO$_2$ Values. Available online: https://www.co2.earth/daily-co2 (accessed on 7 December 2021).
2.　NASA: Global Climate Change: The Relentless Rise of Carbon Dioxide. Available online: https://climate.nasa.gov/climate_resources/24/ (accessed on 7 December 2021).
3.　Urban, M.C. Accelerating extinction risk from climate change. *Science* **2015**, *348*, 571–573. [CrossRef]
4.　Pimm, S.L. Climate disruption and biodiversity. *Curr. Biol.* **2009**, *19*, R595–R601. [CrossRef]
5.　Praksh, G.K.; Olah, G.A.; Licht, S.; Jackson, N.B. Reversing Global Warming: Chemical Recycling and Utilization of CO$_2$. In *Report of the 2008 National Science Foundation-Sponsored Workshop*; University of Southern California: Los Angeles, CA, USA, 2008. Available online: https://loker.usc.edu/ReversingGlobalWarming.pdf (accessed on 7 December 2021).
6.　Yu, M.-F.; Lourie, O.; Dyer, M.; Moloni, K.; Kelly, T.; Ruoff, R. Strength and Breaking Mechanism of Multiwalled Carbon Nanotubes Under Tensile Load. *Science* **2000**, *287*, 637–640. [CrossRef] [PubMed]
7.　Chang, C.-C.; Hsu, H.-K.; Aykol, M.; Hung, W.; Chen, C.; Cronin, S. Strain-induced D band observed in carbon nanotubes. *ACS Nano* **2012**, *5*, 854–862. [CrossRef]
8.　Licht, S.; Liu, X.; Licht, G.; Wang, X.; Swesi, A.; Chan, Y. Amplified CO$_2$ reduction of greenhouse gas emissions with C2CNT carbon nanotube composites. *Mater. Today Sustain.* **2019**, *6*, 100023. [CrossRef]
9.　Kaur, J.; Gill, G.S.; Jeet, K. Chapter 5 Applications of Carbon Nanotubes in Drug Delivery: A Comprehensive Review, in Characterization and Biology of Nanomaterials for Drug Delivery. In *Characterization and Biology of Nanomaterials for Drug Delivery*; Mohapatra, S.S., Ranjan, S., Dasgupta, N., Thomas, S., Eds.; Elsevier: Amsterdam, The Netherlands, 2019; Volume 1, pp. 113–135.
10.　Yang, H.; Xu, W.; Liang, X.; Yang, Y.; Zhou, Y. Carbon nanotubes in electrochemical, colorimetric, and fluorimetric immunosensors and immunoassays: A review. *Microchim. Acta* **2020**, *187*, 206. [CrossRef] [PubMed]
11.　Moghaddam, H.K.; Maraki, M.R.; Rajaei, A. Application of carbon nanotubes(CNT) on the computer science and electrical engineering: A review. *Int. J. Reconfig. Embed. Syst. (IJRES)* **2020**, *9*, 61–82. [CrossRef]
12.　Sehrawat, P.; Julien, C.; Islam, S.S. Carbon nanotubes in Li-ion batteries: A review. *Mater. Sci. Eng. B* **2016**, *213*, 12–40. [CrossRef]
13.　Han, T.; Nag, A.; Mukhopadhyay, S.C.; Xu, Y. Carbon nanotubes and its gas-sensing applications: A review. *Sens. Actuators A* **2019**, *291*, 107–143. [CrossRef]
14.　Kumar, S.; Pavelyev, V.; Tripathi, N.; Platonov, V.; Sharma, P.; Ahmad, R.; Mishra, P.; Khosla, A. Review—Recent Advances in the Development of Carbon Nanotubes Based Flexible Sensors. *J. Electrochem. Soc.* **2020**, *167*, 047506. [CrossRef]
15.　Abdullah, Z.; Othman, A.; Mwabaidur, S. Application of Carbon Nanotubes in Extraction and chromotographic analysis: A review. *Arab. J. Chem.* **2019**, *12*, 633–651.
16.　Basheer, B.V.; George, J.; Siengchin, S.; Parameswaranpillai, J. Polymer grafted carbon nanotubes—Synthesis, properties, and applications: A review. *Nano-Struct. Nano-Objects* **2020**, *22*, 100429. [CrossRef]
17.　Imtiaza, S.; Siddiqa, M.; Kausara, A.; Munthaa, S.J.; Ambreenb, I.B. A Review Featuring Fabrication, Properties and Applictions of Carbon Nanotubes (CNTs) Reinforced Polymer and Epoxy Nanocomposites. *Chin. J. Polym. Sci.* **2018**, *36*, 445–461. [CrossRef]
18.　Gantayata, S.; Routb, D.; Swain, S.K. Carbon Nanomaterial–Reinforced Epoxy Composites: A Review. *Polym.-Plast. Technol. Eng.* **2018**, *57*, 1–16. [CrossRef]
19.　Rafiquea, I.; Kausara, A.; Anwara, Z.; Muhammad, B. Exploration of Epoxy Resins, Hardening Systems, and Epoxy/Carbon Nanotube Composite Designed for High Performance Materials: A Review. *Polym.-Plast. Technol. Eng.* **2016**, *55*, 312–333. [CrossRef]
20.　Kausara, A.; Rafiquea, I.; Muhammad, B. Review of Applications of Polymer/Carbon Nanotubes and Epoxy/CNT Composites. *Polym.-Plast. Technol. Eng.* **2016**, *55*, 1167–1191. [CrossRef]
21.　Shahidi, S.; Moazzenchi, B. Carbon nanotube and its applications in textile industry—A review. *J. Text. Inst.* **2018**, *109*, 1653–1666. [CrossRef]
22.　Rather, S.U. Preparation, characterization and hydrogen storage studies of carbon nanotubes and their composites: A review. *Int. J. Hydrogen Energy* **2020**, *45*, 3847–5110. [CrossRef]
23.　Selvaraja, M.; Haia, A.; Banata, F.; Haijab, M. Application and prospects of carbon nanostructured materials in water treatment: A review. *J. Water Process Eng.* **2020**, *33*, 100996. [CrossRef]
24.　Bassyouni, M.; Mansi, A.E.; Elgabry, A.; Ibrahim, B.A.; Kassem, O.A.; Alhebeshy, R. Utilization of carbon nanotubes in removal of heavy metals from wastewater: A review of the CNTs' potential and current challenges. *Appl. Phys. A* **2020**, *126*, 38. [CrossRef]
25.　Ghoranneviss, M.; Elahi, A.S. Review of carbon nanotubes production by thermal chemical vapor deposition technique. *Mol. Cryst. Liq. Cryst.* **2016**, *629*, 158–164. [CrossRef]
26.　Shah, K.A.; Tali, B.A. Synthesis of carbon nanotubes by catalytic chemical vapour deposition: A review on carbon sources, catalysts and substrates. *Mater. Sci. Semicond. Process.* **2016**, *41*, 67–82. [CrossRef]
27.　Khanna, V.; Bakshi, B.R.; Lee, L.J. Carbon Nanofiber Production: Life cycle energy consumption and environmental impact. *J. Ind. Ecol.* **2008**, *12*, 394–410. [CrossRef]

28. Hu, L.; Song, H.; Ge, J.; Zhu, J.; Jiao, S. Capture and electrochemical conversion of CO_2 to ultrathin graphite sheets in $CaCl_2$-based melts. *J. Mat. Chem. A.* **2015**, *3*, 21211–21218. [CrossRef]

29. Liang, C.; Chen, Y.; Wu, M.; Wang, K.; Zhang, W.; Gan, Y.; Huang, H.; Chen, J.; Zhang, J.; Zheng, S.; et al. Green synthesis of graphite from CO_2 without graphitization process of amorphous carbon. *Nat. Commun.* **2021**, *12*, 119. [CrossRef]

30. Licht, S.; Wang, B.; Ghosh, S.; Ayub, H.; Jiang, D.; Ganley, J. New solar carbon capture process: STEP carbon capture. *J. Phys. Chem. Lett.* **2010**, *1*, 2363–2368. [CrossRef]

31. Ren, J.; Li, F.; Lau, J.; Gonzalez-Urbina, L.; Licht, S. One-pot synthesis of carbon nanofibers from CO_2. *Nano Lett.* **2010**, *15*, 6142–6148. [CrossRef] [PubMed]

32. Ren, J.; Licht, S. Tracking airborne CO_2 mitigation and low cost transformation into valuable carbon nanotubes. *Sci. Rep.* **2016**, *6*, 27760. [CrossRef]

33. Ren, J.; Lau, J.; Lefler, M.; Licht, S. The minimum electrolytic energy needed to convert carbon dioxide to carbon by electrolysis in carbonate melts. *J. Phys. Chem. C.* **2015**, *119*, 23342–23349. [CrossRef]

34. Licht, S.; Douglas, A.; Ren, J.; Carter, R.; Lefler, M.; Pint, C.L. Carbon nanotubes produced from ambient carbon dioxide for environmentally sustainable lithium-ion and sodium ion battery anodes. *ACS Cent. Sci.* **2016**, *2*, 162–168. [CrossRef]

35. Dey, G.; Ren, J.; El-Ghazawi, O.; Licht, S. How does an amalgamated Ni cathode affect carbon nanotube growth? A density functional calculation of nucleation and growth. *RSC Adv.* **2016**, *122*, 400–410.

36. Ren, J.; Johnson, M.; Singhal, R.; Licht, S. Transformation of the greenhouse gas CO_2 by molten electrolysis into a wide controlled selection of carbon nanotubes. *J. CO_2 Util.* **2017**, *18*, 335–344. [CrossRef]

37. Johnson, M.; Ren, J.; Lefler, M.; Licht, G.; Vicini, J.; Licht, S. Data on SEM, TEM and Raman spectra of doped, and wool carbon nanotubes made directly from CO_2 by molten electrolysis. *Data Br.* **2017**, *14*, 592–606. [CrossRef] [PubMed]

38. Johnson, M.; Ren, J.; Lefler, M.; Licht, G.; Vicini, J.; Liu, X.; Licht, S. Carbon nanotube wools made directly from CO_2 by molten electrolysis: Value driven pathways to carbon dioxide greenhouse gas mitigation. *Mater. Today Energy* **2017**, *5*, 230–236. [CrossRef]

39. Wang, X.; Liu, X.; Licht, G.; Wang, B.; Licht, S. Exploration of alkali cation variation on the synthesis of carbon nanotubes by electrolysis of CO_2 in molten carbonates. *J. CO_2 Util.* **2019**, *18*, 303–312. [CrossRef]

40. Wang, X.; Licht, G.; Licht, S. Green and scalable separation and purification of carbon materials in molten salt by efficient high-temperature press filtration. *Sep. Purif. Technol.* **2021**, *244*, 117719. [CrossRef]

41. Wang, X.; Sharif, F.; Liu, X.; Licht, G.; Lefer, M.; Licht, S. Magnetic carbon nanotubes: Carbide nucleated electrochemical growth of ferromagnetic CNTs. *J. CO_2 Util.* **2020**, *40*, 101218. [CrossRef]

42. Wang, X.; Liu, X.; Licht, G.; Licht, S. Calcium metaborate induced thin walled carbon nanotube syntheses from CO_2 by molten carbonate electrolysis. *Sci. Rep.* **2020**, *10*, 15146. [CrossRef]

43. Liu, X.; Licht, G.; Licht, S. The green synthesis of exceptional braided, helical carbon nanotubes and nanospiral platelets made directly from CO_2. *Mat. Today Chem.* **2021**, *22*, 100529. [CrossRef]

44. Liu, X.; Licht, G.; Licht, S. Data for the green synthesis of exceptional braided, helical carbon nanotubes and nano spiral platelets made directly from CO_2. *arXiv* **2021**, arXiv:2110.05398.

45. Lau, J.; Dey, G.; Licht, S. Thermodynamic assessment of CO_2 to carbon nanofiber transformation for carbon sequestration in a combined cycle gas or a coal power plant. *Energy Convers. Manag.* **2016**, *122*, 400–410. [CrossRef]

46. Licht, S. Co-production of cement and carbon nanotubes with a carbon negative footprint. *J. CO_2 Util.* **2017**, *18*, 378–389. [CrossRef]

47. Liu, X.; Ren, J.; Licht, G.; Wang, X.; Licht, S. Carbon nano-onions made directly from CO_2 by molten electrolysis for greenhouse gas mitigation. *Adv. Sustain. Syst.* **2019**, *3*, 1900056. [CrossRef]

48. Ren, J.; Yu, A.; Peng, P.; Lefler, M.; Li, F.-F.; Licht, S. Recent advances in solar thermal electrochemical process (STEP) for carbon neutral products and high value nanocarbons. *Acc. Chem. Res.* **2019**, *52*, 3177–3187. [CrossRef] [PubMed]

49. Liu, X.; Wang, X.; Licht, G.; Licht, S. Transformation of the greenhouse gas carbon dioxide to graphene. *J. CO_2 Util.* **2020**, *36*, 288–294. [CrossRef]

50. Wang, X.; Licht, G.; Liu, X.; Licht, S. One pot facile transformation of CO_2 to an unusual 3-D nan-scaffold morphology of carbon. *Sci Rep.* **2020**, *10*, 21518. [CrossRef] [PubMed]

51. Liu, X.; Licht, G.; Licht, S. Controlled Transition Metal Nucleated Growth of Unusual Carbon Allotropes by Molten Electrolysis of CO_2. *Catalysts* **2022**, *12*, 125. [CrossRef]

52. Gui, X.; Wei, J.; Wang, K.; Cao, A.; Zhu, H.; Jia, Y.; Shu, Q.; Wu, D. Carbon nanotube sponges. *Adv. Mat.* **2010**, *22*, 617–621. [CrossRef] [PubMed]

53. Yu, S.-H. Carbon nanofiber aerogels for emergent cleanup of oil spillage and chemical leakage under harsh conditions. *Sci. Rep.* **2014**, *4*, 4079.

54. Kim, K.H.; Tsui, M.N.; Islam, M.F. Graphene-Coated Carbon Nanotube Aerogels Remain Superelastic while Resisting Fatigue and Creep over −100 to +500 °C. *Chem. Mater.* **2017**, *4*, 2748–2755. [CrossRef]

55. Wan, W.; Zhang, R.; Li, W.; Liu, H.; Lin, Y.; Li, L.; Zhou, Y. Graphene–carbon nanotube aerogel as an ultra-light, compressible and recyclable highly efficient absorbent for oil and dyes. *Environ. Sci. Nano* **2016**, *3*, 107–113. [CrossRef]

56. Ozden, S.; Narayanan, T.N.; Tiwary, C.S.; Dong, P.; Hart, A.H.; Vajtai, R.; Ajayan, P.M. 3D macroporous solids from chemically cross-linked carbon. *Small* **2015**, *11*, 688–693. [CrossRef] [PubMed]

57. Schaefer, A.; Fane, A.G.; Waite, T.D. *Nanofiltration: Principles and Applications*; Elsevier: Oxford, UK, 2005.

58. Marchetti, P.; Jimenez Solomon, M.F.; Szekely, G.; Livingston, A.G. Molecular Separation with Organic Solvent Nanofiltration: A Critical Review. *Chem. Rev.* **2014**, *114*, 10735–10806. [CrossRef] [PubMed]
59. Qu, H.; Rayabharam, A.; Wu, X.; Wang, P.; Li, Y.; Fagan, J.; Aluru, N.R.; Wang, Y. Selective filling of n-hexane in a tight nanopore. *Nat Commun.* **2021**, *12*, 310. [CrossRef]
60. Hashim, D.P.; Romo-Herrera, J.M.; Muñoz Sandoval, E.; Ajayan, P.M. Covalently bonded three-dimensional carbon nanotube solids via boron induced nanojunctions. *Sci. Rep.* **2012**, *2*, 363. [CrossRef]
61. Gabay, T.; Jacobs, E. Engineered self-organization of neural networks using carbon nanotube clusters. *Physica A* **2005**, *350*, 611–621. [CrossRef]
62. Licht, S. Carbon Dioxide to carbon nanotube scale-up. *arXiv* **2017**, arXiv:1710.07246.
63. XPrize Foundation. *Turning CO$_2$ into Products*; XPrize Foundation: Culver City, CA, USA, 2021. Available online: http://CarbonXPrize.org (accessed on 14 December 2021).
64. XPrize Announces Winners with Each Team Creating Valuable Products from CO$_2$. Available online: https://www.nrg.com/about/newsroom/2021/xprize-announces-the-two-winners-of--20m-nrg-cosia-carbon-xprize.html (accessed on 14 December 2021).